Mineralogy, Geochemistry and Raman Spectroscopy of Multi-Genesis Serpentine Polymorphs of Darepahn Ophiolites

B. Bahrambeygi[1], H. Moeinzadeh[*1], S.K. Alavipanah[2]

[1] Department of Geology, Faculty of Sciences, Shahid Bahonar University of Kerman, Kerman, Islamic Republic of Iran
[2] Department of Remote sensing and GIS, Faculty of Geography, University of Tehran, Tehran, Islamic Republic of Iran

Abstract

The present article pays to some Alpine-Himalayan ophiolites of Late Cretaceous age from Darepahn area in the southern part of Nain-Baft Ophiolite belt. Whole rock processed data clearly shows that the metaperidotite rocks are silica-poor with low CaO, Al_2O_3, and TiO_2 that reflect the predominance of olivine over calcic pyroxene in the protolithes. The considerable content of Co (85.6–124.6 ppm) and very low contents of Sc (4.3–15.3 ppm) and Sr (0.7-14 ppm) provided more evidence for olivine enrichment in the rock parentages. Calculating numbers of cation per formula unites based on EMPA results for distinguished Serpentine polymorphs (classified structurally via Raman spectroscopy) display that Tschermak substitution of trivalent cations for lizardite is tetrahedrally, and for chrysotile and antigorite, it is octahedrally. These chemical differentiations, lead to identifying chemical field plots in separator diagrams between SiO_2, MgO, H_2O, and Al_2O_3. Lizardite polymorphs can consider as primarily metasomatism results thru an iron-rich fluid occurrence. It has a considerable occupation of trivalent cations (especially Fe^{3+}) and simultaneous less than 4 Si atoms in formula structure that reflected tetrahedral Tschermak substitutions. Antigorites have some deformed recrystallized textures along with high Σoct (Total Octahedral Cations) and low H_2O content that could be considered as thermal originated polymorph. Chrysotiles have bimodal MgO and FeO contents that return to magnetite formations in groundmass and octahedral Tschermak substitutions on late-stage veins. The results exemplify compositional variations of Darepahn Serpentine polymorphs as a function of textural behaviors, structural position and thermodynamic condition of the formation process.

Keywords: Darepahn; Alpine-Himalayan Ophiolite; Serpentine polymorphs; Metaperidotites; Raman spectroscopy.

Introduction

A perfect identification of serpentine polymorph types using optical-chemical characters is a problematic issue yet [1, 2]. However, some common microstructure properties but mineral chemistry characteristics of serpentine group minerals are variable in different ophiolitic belts. The present study gives the first

* Corresponding author: Tel: +989131414103; Fax: +983431322232; Email: hmoeinzadeh@uk.ac.ir

detailed information about microstructures and mineral chemistry of serpentine-group minerals in Darepahn area as a Late Cretaceous serpentinite from the southern area of the ophiolitic belt of Nain-Baft. We are presenting detailed geochemical and mineralogical characteristics of local serpentine minerals to distinguish polymorphs based on spot point chemical and laser spectral analysis methodology. The combined mineralogical, Spectral and chemical records lead to discovering the chemical variations as functions of thermodynamic phase situation of the formation in this local serpentine polymorphs. These outcomes concluded to new chemical diagrams that discriminate different serpentine polymorph types.

Darepahn area is located in the Nain-Baft Ophiolitic zone as a central position of Alpine-Himalayan orogenic belt. The studied area covered with Mantle-derived serpentinized ultramafic rocks that are common lithologies in the hosted regional ophiolitic belt. Studying Metaperidotite and serpentinites from different parts of the area, illustrate the presence of all main serpentine polymorphs in serpentinized rocks of Darepahn area.

In the history of collisional orogenic belts, there are some important steps that could be involved by ophiolitic emplacement. Multiple collisions between microcontinents, interoceanic arc–trench systems, and continents following the closures of ocean basins could be steps include ophiolitic emplacement [3]. One of the most important collisional orogenic belts is the Mesozoic Alpine–Himalayan belt. This collisional orogenic belt commonly displays records of some ophiolitic lithology in variety coordinates such as Iranian Inner Zagros zone.

In the Alpine–Himalayan ophiolitic zones, ultramafic unites are commonly serpentinized. The process of serpentinization based on thermodynamic phase conditions thru deformation steps will cause the formation of different serpentine polymorphs of antigorite, lizardite, and chrysotile [4]. Serpentinization is a process that is characterized by dissolution-precipitation and reduction-oxidation reactions when the ultramafic rocks are fractured and exposed to water at crustal levels. Recent studies e.g. [5, 6] suggest that serpentinization is dominated by incipient hydration that involves a volume increase of ~20–40 %, and it consumes water but does not release any significant dissolved species except for H_2 [7]. When primary silicates alter to serpentines, their density changes from 3.3 to 2.7 g/cm^3 and a considerable increase in volume happens; the net result is a fracture system in which newly formed serpentine minerals, particularly the fibrous type is formed. Because serpentinite does not

expand, it fractures to accommodate the increase in volume [1, 8, 9].

It is pointed out the possible connection of serpentinization and arc magmatism whereas most of the previous literature assigns ocean-floor spreading as a common regime of hydrothermal alteration of ultramafic rocks to form serpentinites [5]. That is reported significant mineralogical differences in serpentinites where magnetite co-existing with antigorite is a common product of ocean-floor serpentinization and this distinguishes them from magnetite-poor mantle wedge serpentinization [1, 10, 11]. The latter is a high-T regime that is characterized by fast diffusion rates of Fe-Mg above 400 °C and thermodynamic equilibrium can be achieved above ~600 °C [10]. It is considered that serpentine minerals with ~13 wt% H_2O as important components in the global subduction zone water cycle and for flux melting in the mantle wedge beneath magmatic arcs [12]. In summary, serpentinization can produce a variety of serpentine minerals, magnetite, Fe-Ni alloys, gases (H_2 and CH_4) and alkaline solutions [13, 14].

Geologic setting

Late Cretaceous ophiolites in the Mediterranean eastward over Turkey, Syria, Iran, Oman, Afghanistan, and Pakistan are slices of neotethyan oceanic lithosphere [15]. The Iranian ophiolite belt, that contains the current study area, lies along the NE flank of the Zagros fold-and-thrust belt, which flanks the Persian Gulf on the southern margin of Eurasia [16]. The Inner Zagros ophiolite belt (that contains Nain-Baft ophiolite belt and Darepahn mélanges in southern parts) occurs in several massifs named after nearby towns. These ophiolites can be traced along strike for ~500–600 km and are stretched from northwest to southeast, the Nain, Dehshir, Shahr-e-Babak, Balvard-Baft and Darepahn ophiolites (Fig. 1). The formation and tectono-magmatic evolution of Inner Zagros ophiolite belt, including the Nain-Baft ophiolites and the Darepahn ophiolite of interest here, are controversial and have been variously interpreted as (1) representing a narrow, Red Sea–like ocean, created at a slow spreading center e.g., [16]; (2) an arc basin related to Tethyan subduction e.g., [17, 18]; and (3) a back-arc basin [19].

Limited geo-chronology information indicates that inner and outer Zagros ophiolitic belts formed at the same time during the Late Cretaceous and may have originally been a continuous sheet [20]. Horn-blende gabbros from the inner belt yield a K/Ar age of 93 Ma [20] , whereas outer belt Neyriz diabases and hornblende gabbros yield 40Ar/39Ar ages of 86 and
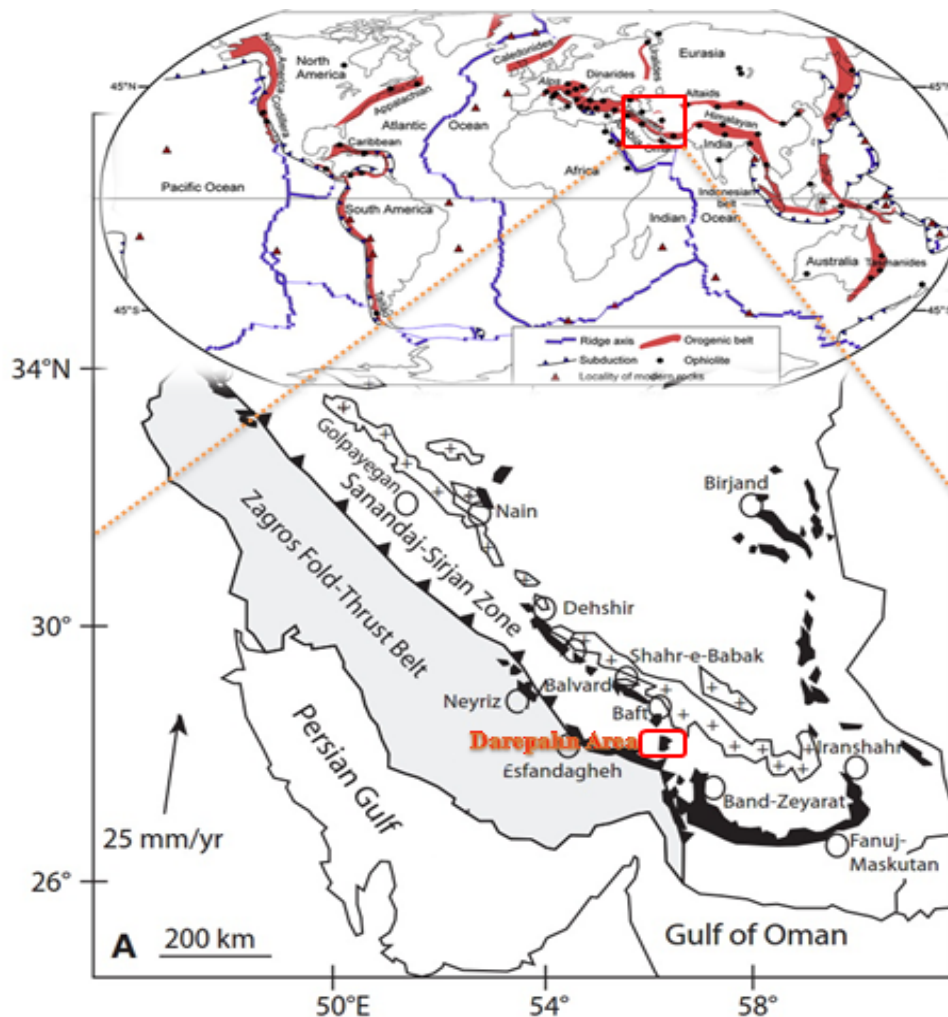
Figure 1. location of Darepahn area on the distribution map of thethe Iranian ophiolite belts amongst global Alpine – Himalayan collisional belt. Main Zagros thrust, detached inner and outer Zagros ophiolites and Darepahn is located in inner Zagros ophiolitic belt (with modifying from [16]).

93 Ma, respectively [21], and Neyriz hornblende gabbros yield 40Ar/39Ar ages of 92.1 ± 1.7 Ma and 93.2 ± 2.5 Ma [22]. These are broadly similar to ages of other ophiolites of the Mediterranean-Oman belt, which get younger toward the west, from 95 Ma for Oman [23] to 90–94 Ma for Cyprus [24]. The similarity of ages for inner and outer belt ophiolites and their parallel alignment between the Urumieh-Dokhtar arc and the Zagros fold-and-thrust belt suggest that they may be exposed limbs of a deformed and eroded anticlinoria, and may represent fore-arc basement between the Urumieh-Dokhtar arc and the Zagros accretionary prism, developed over a N-dipping subduction zone on the southern Eurasian margin.

Local geological outline

The Darepahn area has been previously described mainly as part of inner Zagros belt in regional geological mapping [25]. The study area as southern part of Nain-Baft ophiolites can be considered as a part of inner Zagros ophiolites with age and a tectonomagmatic situation similar to Nain-Baft and Dehshir ophiolites. In this paper, petrography, mineralogy, mineral chemistry, and geochemical investigations were done on serpentinite and Metaperidotites of Darepahn ophiolite mélanges, which is exposed in the south of the Urumieh-Dokhtar magmatic arc (Fig. 1). Darepahn Ophiolite massive similar to other massifs of the inner part of Zagros ophiolites contain the components of a complete stratigraphic column of "Penrose ophiolites," [26] including tectonized harzburgites, gabbros, and pillowed basalts. Sheeted dike complexes and mafic cumulates are rare. All the massifs in the Inner Zagros

ophiolite belt are overlain by Turonian-Maastrichtian pelagic limestones (93.5–65.5 Ma), consistent with the limited geochronologic evidence that these ophiolites formed by seafloor spreading with age of 90–95 Ma [16]. Several lines of evidence, such as high Cr content (Cr# > 60) of spinel in harzburgite, flat rare earth element (REE) patterns of the lavas, Nb-Ta negative anomalies and large positive ion lithophile element (LILE) anomalies, and the presence of low-Ti in Clino-pyroxenes in the lavas, indicate that the Inner Zagros ophiolite belt forming above a subduction zone [17, 18, 27]. Figure 2 shows a local map of Darepahn area that exposes discontinuously over ~350 km^2, near the southern part of the Inner Zagros ophiolite belt. It consists of the oceanic mantle and crustal

sequences that include mixed melanges of meta-harzburgites, serpentinized peridotites along with some rare sheeted dikes in unite presented as serpentinite and metaperidotites. Pillow lava have acourances in parts named as spilitized basalts. These lithology compositions agrees with [25, 28] that presented for all Inner Zagros ophiolites. As illustrated in Figure 2. Darepahn area is intensively tectonized with more than 50 detectable linear structures and faults that show a complex deformation history. Lithology is cluttered and mixed up so that just relatively dominant ratio of some lithology than others can consider as a reason for separate it from others in a district. Despite irregular lithology distribution, in the current study same serpentinized peridotites were sampled and investigated.
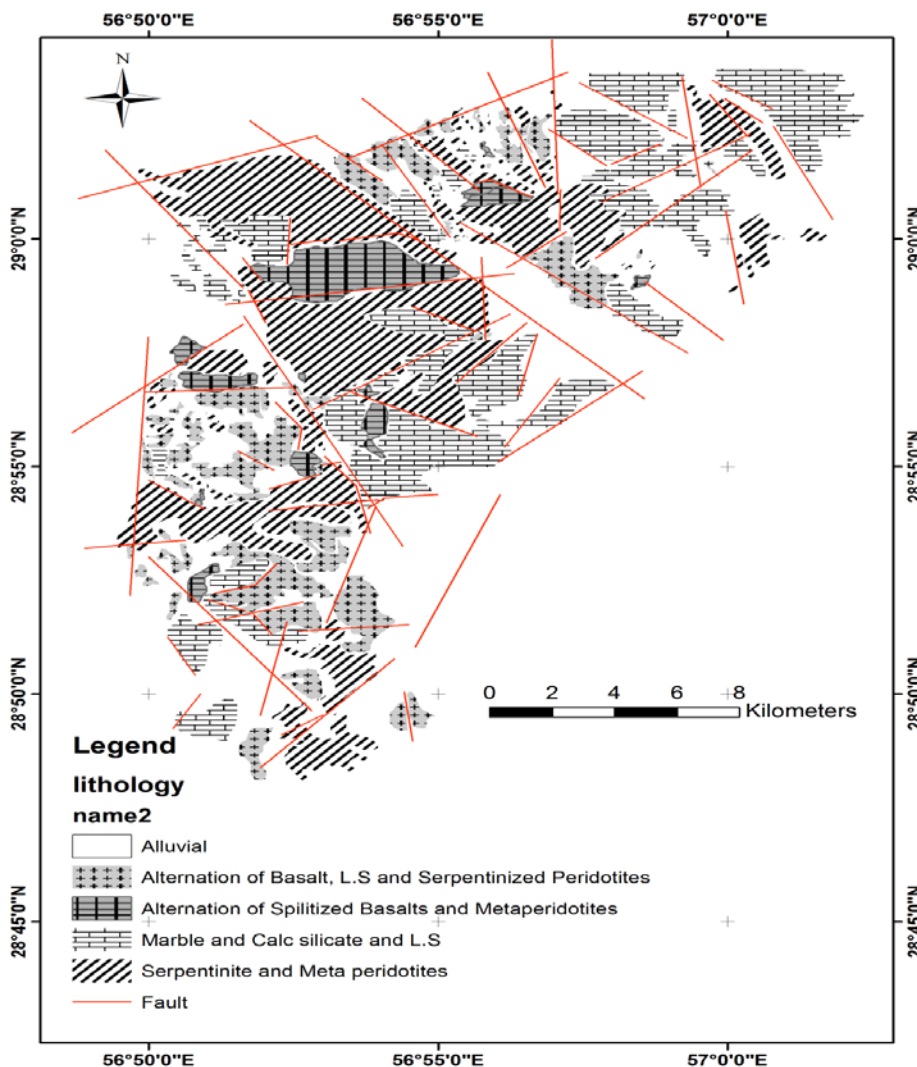

Figure 2. local geological map of Darepahn are, Lithologies are cluttered and mixed up so that just relatively dominant ratio of some lithology than others considered as a reason for the distinction.

There are some geochemical and mineralogical variations in same lithologies that indicate evidence of different metamorphism and metasomatism processes.

Materials and Methods

In order to identify rock types, rock forming minerals, textural features, and especially serpentine mineral characteristics, more than 100 local samples were analyzed. Samples were taken from all serpentinized-ultramafic outcrops in the Darepahn area district. The microscopic investigation and the analytical works were done in Iran and Austria respectively at the Department of Geology of the University of Bahonar-Kerman and Department of Lithospheric Sciences of the University of Vienna. The whole-rock composition was measured by the XRF machine use Philips PW2400 spectrometer for major and selected trace element analysis in Department of Lithospheric Sciences of the University of Vienna. The XRD runs were done using a Bruker D8-Advance powder X-ray diffract meter, the theta-theta type with a scintillation counter, energy-dispersive Sol-X or position sensitive Lynx-Eye detector and 105 position sample changer, attachments for a Paar XRK900 reaction chamber (298 - 1173 K) in the department of mineralogy and crystallography of University of Vienna. The machine used for the EMPA and spot chemical analyses of minerals is an electron X-ray micro analyzer (Camera SX50) working at accelerating voltages up to 30kV and beam currents up to 200nA for the electron beam and 1pA to 65nA for the ion-beam sample current. The used standards represent a set of natural oxides with the exception of synthetic nickel metal for Ni. The obtained data were normalized using oxygen and cation NORM programs. Raman spectroscopy was recorded by Horiba Jobin Yvon LabRAM-HR 800 spectrometer, a confocal micro-Raman system with 473/532/633 nm laser excitation, z-focus, and a software-controlled x-y sample stage for line scanning and mapping. Based on [29] the best Raman laser excitation for serpentine polymorphs distinguishing is 532 nm, so we used laser excitation of 532 nm on selected serpentine minerals.

Results and Discussion

Petrographic investigation of the studied serpentinites from all district localities illuminated the existence of both pseudomorphic and non-pseudomorphic textures as defined by [30]. A perfect identification of serpentine polymorph types using optical characters is a problematic issue yet [2], however, there are some relative qualities that could be used to separate polymorph types [31]. One of the best methods for serpentine polymorph identification is Raman laser beam analyses [29] that were used for this study. The common background matrix consists of antigorite whereas the chrysotiles are common in veins and Lizardites are common forms in Olivine pseudomorphs. In the studied serpentinites, the pseudomorphic textures are represented by mesh-textured and bastite serpentines. Mesh-textured serpentines consist of lizardite polymorphs and developed after olivine alteration (Fig. 3a-b). Bastites developed on pyroxene pseudomorphs. Bastite is not a distinct serpentine polymorph but a term applied to mineral aggregates of pyroxene pseudomorphs [32]. In the current samples, bastites commonly consisted of antigorite polymorphs. Non pseudomorphic textures show the characteristics of antigorite with several textural forms such as fibrous, interlocking and massive texture. The transition textures are common too. In some cases, antigorite is replaced by lizardite that caused to brucite formation (Fig. 3g). There is some retrograde product of both pseudomorphic and non-pseudomorphic serpentines that are dominant during the late stages of serpentinization [30]. In the studied serpentine evolution history, there were a thermally stage that fibrous antigorite was deformed and resized to larger antigorites (Fig. 3c) as it replaces finer former antigorite (Fig. 3d). Thermal stage hypothesis is supporting with mineral chemistry information too. Bastites are common pseudomorph in samples that consist of replaced antigorites (Fig. 3c-d-h). In rarely cases there is minor value Tremolite in some altered samples (Fig. 3h). Addition minerals are relict magmatic Cr-spinels anyway whether the rock is regionally or thermally metamorphosed. Magnetite is irregular and maybe results from the breakdown of ferromagnesian minerals during serpentinization. A summary of the mineralogy that characterizes the Darepahn serpentinites is given in Table 1.

Whole-rock geochemistry of serpentinites

Protolith identification of Alpine type peridotites is an important issue in petrogenesis investigation [33]. However whole rock geochemistry of serpentinites can be used to obtain information on the protolithes, but it should be considered that serpentinization is a metasomatic process that involves some mobile certain elements [34]. XRF analyses of some representative serpentinized peridotites from the study area are given in Table 2. These data clearly show that the analyzed rocks are silica-poor with 36.52 to 41.34 wt. % SiO_2. The low CaO contents (0.06–2.06) likely reflect the predominance of olivine over calcic pyroxene in the protolithes. As the major oxides such as MgO, CaO, and
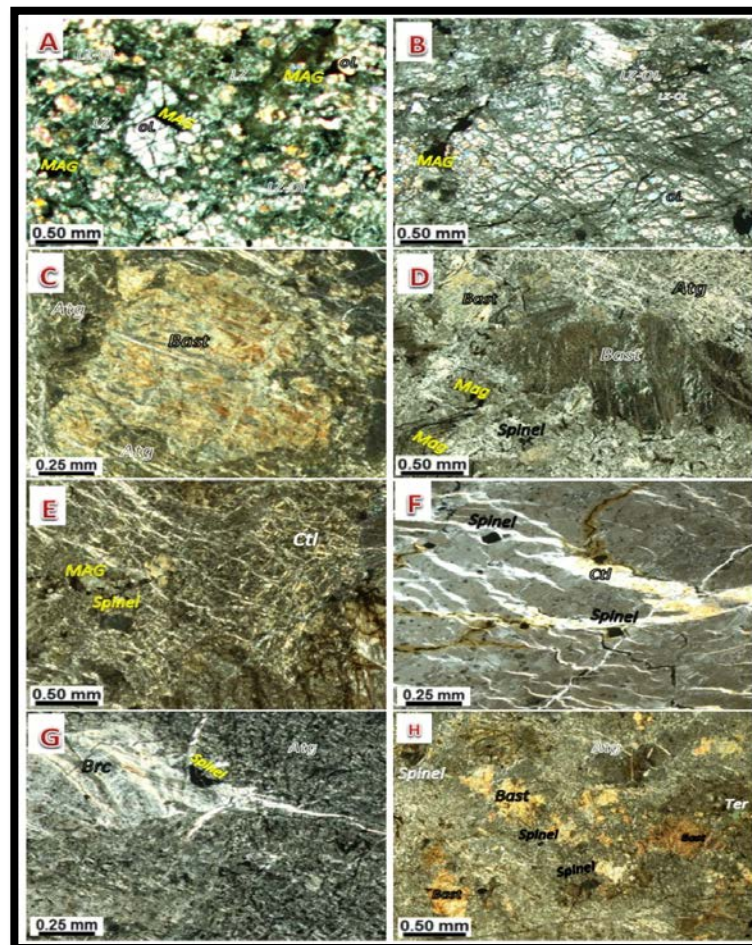
Figure 3. Petrographic characteristics of the studied Darepahn serpentinites. All microphotographs were taken with crossed-nicols. Abbreviations are after[55].

A and B: Mesh textured serpentinite made up of lizardite (Lz) with Olivine (Ol) and Spinel relict minerals and replaced Magnetite (Mag) as metasomatism results.

C and D: Fibrous antigorites replaced on orthopyroxene pseudomorphs as Bastite (Bast) and Growth of thermal antigorite at the background with the expense of finer-grained regional antigorite from the southern area.

E: Dense aggregates of chrysotile (Ctl) with spinel relicts and some replaced Magnetite. The serpentinites from Central parts

F: Chrysotile originated in cracks in the mass antigorite background with spinel relict minerals.

G: Recrystallized massive antigorite (Atg) along with Brucite (Barc) with Spinel and replace magnets (Mag). Crack-seal brucite (Brc) within antigorite.

H: Recrystallized Antigorite, and pseudomorphic OPX replaced by fibrous antigorite as Bastite in thermally metamorphosed serpentinites from the southern area. Some Tremolite & spinel relicts are detectable in the background too.

FeO in serpentinites are problematic for identifying original protolith (because of their high mobility and possible leaching or addition to the surrounding lithologies) [46] we used less mobile elements.

The studied serpentinites are Al_2O_3 - and TiO_2 -poor (up to 2.39 and 0.07, respectively) that represent a dunite-peridotite and not pyroxenite protolith for the majority of serpentinites in the study area. This is clear on the S-M-F diagram (Fig. 4a). Protolithes are plotted in the Alpine-type ultramafic rocks on the Cr2O3-NiO diagram that implying their exclusive ophiolitic nature

(Fig. 4b).

The less mobile trace elements (Table 2) can also be helpful for constraining the serpentinite original parentage. Low contents of Sc (4.3–15.3 ppm) and Sr (0.7-14 ppm) are consistent with a parentage that lacks pyroxenite. On the other hand, the considerable content of Co (85.6–124.6 ppm) is another support for olivine enrichment parentage of studied rocks. Ternary diagram of Co, V, and Zn in Figure 4c shows that the most serpentinites in the Darepahn are derived from dunite harzburgite parentages however there are a few samples

Table 1. Mineralogy of the studied serpentinites from Darepahn Melanges based on petrography, Raman spectroscopy and XRD data (PSD.Tex: Pseudomorphic texture - NPSD.Tex: None-Pseudomorphic texture - R: Rare- VR: Very rare- C: Common- VC: Very common- A: Absence)

| No. sample.	PSD.Tex	NPSD.Tex	Bastite	Antigorite	lizardite	Chrysotile	Olivine	Pyroxene	Spinel	Magnetite	Tremolite	Brucite
1 BP-32	50	50	R	C	VC	R	VC	R	R	R	A	A
2 BP-11	15	85	C	VC	A	R	A	C	R	R	A	R
3 BP-12	30	70	C	VC	R	C	A	C	R	R	A	R
4 BP-45	40	60	C	VC	R	C	A	C	C	C	A	A
5 BP-46	25	75	C	VC	R	C	R	C	C	C	A	A
6 BP-19	15	85	R	VC	R	C	A	R	R	VR	A	R
7 BP-411	30	70	R	VC	R	R	R	R	R	R	A	R
8 BP-6	10	90	R	VC	A	C	A	R	C	R	R	R
9 BP-9	20	80	A	VC	A	R	A	A	R	R	R	A
10 BP-43	40	60	R	VC	R	C	A	R	R	R	R	R
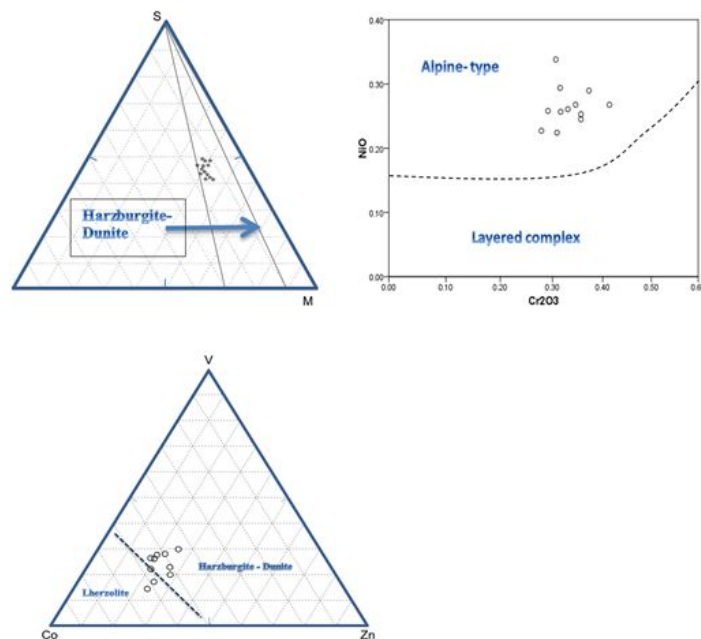
Figure 4. Lherzolite-harzburgite parentage of the Alpine-type or ophiolitic nature of the Darepahn serpentinites based on their whole rock composition.

A: SFM ternary diagram of Pfeifer (1979) where $S = SiO_2 + Al_2O_3 + Na_2O$, $F = FeO + CaO + Al_2O_3 + 2Na_2O$ and $M = MgO + CaO + Al_2O_3 + 2Na_2O$.

B: Cr_2O_3 vs. NiO binary diagram of Irvine and Findlay (1972).

C: Trace elements ternary diagram of Pfeifer (1979)

that plotted in lherzolite derivation field. By geographical investigation, we noticed that these limited samples are related to the southern district of the study area. So dominantly protolithes are Olivine-rich magmatic parentages (Dunite-Harzburgite) with a few southern serpentinite samples that could be derived from lherzolites.

Raman spectroscopy

The three principal minerals of the serpentine group (chrysotile, antigorite, and lizardite) are known as very similar chemical composition, but significantly different structures. Naturally occurring intergrowths of three types of serpentine minerals are very complexity [10]. It is thus of great interest to find an experimental

Table 2. Whole-rock XRF analyses of serpentinites from Darepahn ophiolitic area Major Oxides in %

Sample	BP-11	BP-12	BP-19	BP-32	BP-411	BP-6	BP-9	BP-43	BP-45	BP-46
SiO_2	39.06	39.20	38.32	38.84	37.12	41.34	38.95	40.00	38.17	36.52
TiO_2	0.02	0.02	0.02	0.07	0.01	0.01	0.02	0.03	0.01	0.00
Al_2O_3	0.97	0.92	1.41	2.00	0.99	0.76	1.07	1.59	1.00	0.59
Fe2O3	8.71	8.71	8.49	9.65	8.92	10.13	8.73	10.34	9.58	10.15
MnO	0.11	0.11	0.14	0.15	0.16	0.12	0.11	0.16	0.18	0.15
MgO	35.67	35.49	35.53	35.09	36.34	33.18	35.24	33.02	35.08	37.15
CaO	1.13	1.43	1.01	2.03	0.07	0.45	1.27	0.27	0.16	0.06
Na2O	0.14	0.00	0.13	0.25	0.16	0.14	0.19	0.12	0.18	0.00
K2O	0.01	0.00	0.00	0.01	0.01	0.01	0.01	0.01	0.01	0.00
P2O5	0.00	0.00	0.00	0.01	0.00	0.01	0.00	0.00	0.06	0.00
SO3	0.36	0.32	0.36	0.21	0.15	0.03	0.37	0.02	0.45	0.37
NiO	0.25	0.22	0.27	0.23	0.26	0.29	0.27	0.29	0.26	0.34
Cr2O3	0.36	0.31	0.35	0.28	0.29	0.31	0.41	0.37	0.33	0.31
LOI	13.15	13.16	13.79	10.93	15.40	13.10	13.26	13.68	14.38	14.30
Total	99.41	99.46	99.39	99.44	99.43	99.36	99.34	99.34	99.40	99.38

				Minor elements in ppm						
Sample	BP-11	BP-12	BP-19	BP-32	BP-411	BP-6	BP-9	BP-43	BP-45	BP-46
Ba	0.5	3.5	0.3	1.8	3	0.5	4.8	0.5	0.5	3.7
Ce	9.1	2.1	6.7	2	4.3	0.5	3.6	0.8	2.7	6.8
Co	96.5	85.6	99.5	93.3	99	113.3	99.3	99.9	101.5	124.6
Cr	2439.1	2114.7	2365.6	1907.2	1994.3	2156.2	2832.5	2549.1	2260.7	2099.3
Cu	22.1	23	22	29.1	17	17.1	28	25.7	28.2	15.8
Ga	1	0.7	1.3	1.9	0.6	2.4	0.9	2.7	0.9	0.8
La	1	0.5	0.2	3.3	0.5	0.5	0.1	0.5	0.5	0.5
Mo	0.1	0.2	0.5	0.2	0.5	0	0	0.2	0	0.2
Nb	0.5	0.5	0.5	0.5	0.5	0.5	0.5	0	0.5	0
Nd	0.8	2.1	4.2	5.9	4.7	0.5	0.5	0.5	2	0.7
Ni	1992	1765.3	2108.4	1788.8	2032.7	2315.1	2107.7	2281.5	2053.5	2662.2
Pb	1	0.5	0.7	0.9	0.6	1	1	1.6	1.1	1.1
Rb	0	0	0.1	0.1	0	0.1	0	0.1	0	0
Sc	6.4	4.3	11.1	7.6	9	8.6	5.8	15.3	10.6	9.1
Sn	3.9	1.9	3.4	2.7	2.2	3.4	3.2	2.2	0.9	3.2
Sr	2.5	2.2	5.3	5.9	2.4	13.9	2.7	11.8	2.7	0.7
Ta	1.3	0.5	0.3	1.3	1.2	0.8	0.8	1.5	1.6	0.5
Th	0.1	0.2	0.3	0.5	0	0.1	0.1	0.6	0.5	0.6
U	0.5	0.2	0.5	0.5	0.5	0.2	0.5	0.2	0.5	0
V	37.4	41.7	52.6	52.5	38	33.2	47.6	67.1	45.9	28.9
W	0.5	0.5	0.5	0.5	0.5	0.5	0.5	0.5	0.5	0.5

technique that permits identification of the mineral species without long and costly preparation of the sample. Raman spectroscopy is a precise, simple and rapid technique, and necessitates no special sample preparation [29]. There are three main peaks in the Raman spectrum of serpentine minerals [35] (Fig. 5). a) The band around of 230 cm^{-1} is a low number main peak of serpentine minerals that return to O-H-O vibrations; b) the band around of 380 cm^{-1} that return to vibrations of the Mg–OH groups; c) the band around of 690 cm^{-1} that attributed to the symmetric stretching mode of the Si–Ob–Si groups [36]. The exact stock line wavenumbers in the defined reasonable range are flexible based on regional lithology characteristics [35, 37]. In the range of these standard identified main peaks, we experimentally obtained specified wave

numbers for Darepahn serpentine samples (Fig. 5). Based on Raman processed data of studied samples, peak wavenumbers that tend to lowest reflect antigorite, moderate wave numbers are returned to lizardite and highest wave numbers in the reasonable range are belongs to chrysotile (Fig. 5 & Fig. 6). Figure 6 shows the histogram distribution of Raman peak wavenumbers in each serpentine polymorph of Darepahn serpentine samples.

Chemical differentiations of serpentine polymorphs

Based on Raman spectroscopic investigations, selected serpentine polymorphs were classified and then analyzed by spot point chemical method of EMPA. The electron microprobe analyses of all serpentines were normalized using the OXYGEN NORM computer
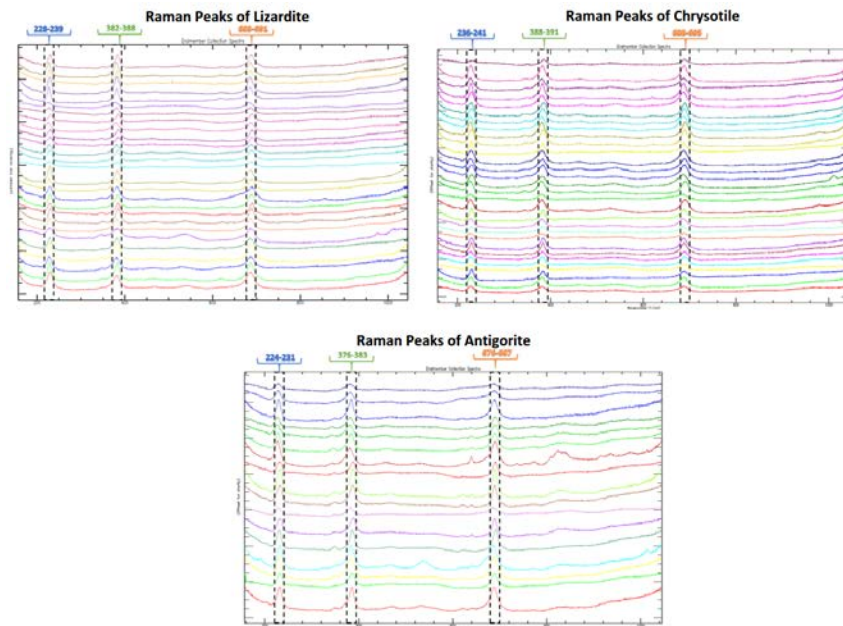
Figure 5. Range of main peak wavenumbers of Raman spectrums for Antigorite, Lizardite and Chrysotile of Darepahn area; Ant has lowest wavenumbers and Chrysotile has the highest
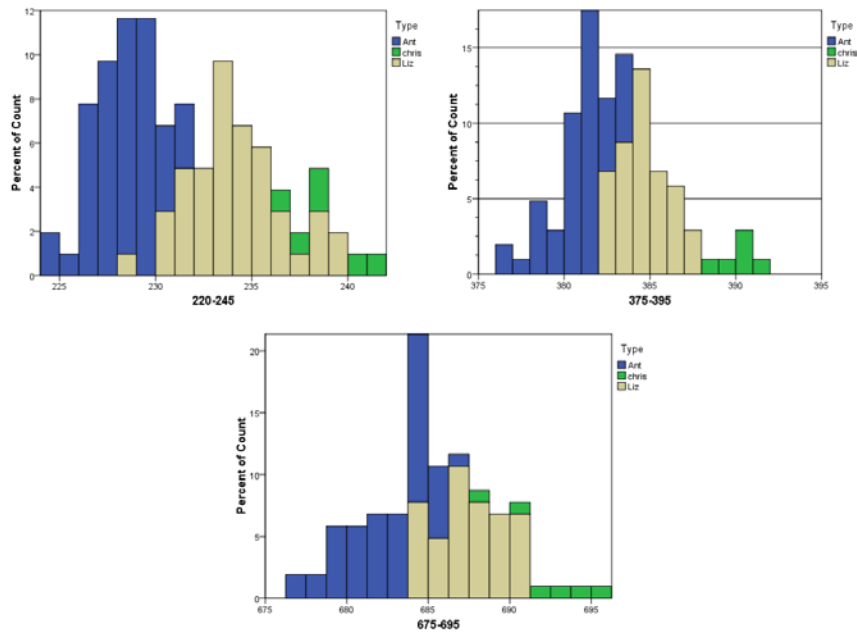

Figure 6. Histogram of 3 main Raman peaks for studied serpentine polymorphs of Darepahn area Peak wave number of 215 to 240; 365to 395; 675 to 695 respectively presented in classified histograms based on serpentine polymprph types. Lizardite, Chrysotile, and Antigorite respectively labeled in Ant, Chrs, and Li.

program on an anhydrous basis of 14 oxygen atoms. Iron is calculated as Fe^{2+} and then excludes the minor Fe^{3+} in the tetrahedral sites that might result in a charge difference [38, 39]. The H_2O was calculated as a difference to the ideal total of 100 wt. %. This approach is more recommended than the calculation of water stoichometrically [1].

Chemical differences among serpentine polymorphs is an accepted issue [38, 40] that is variable based on regional historical phenomena that formed a lithology province [41]. Chemical investigations of classified polymorphs lead to significant separator diagrams to identify studied area serpentine polymorphs (Fig. 7). Polymorph discriminant diagrams of Σoct versus SiO_2,
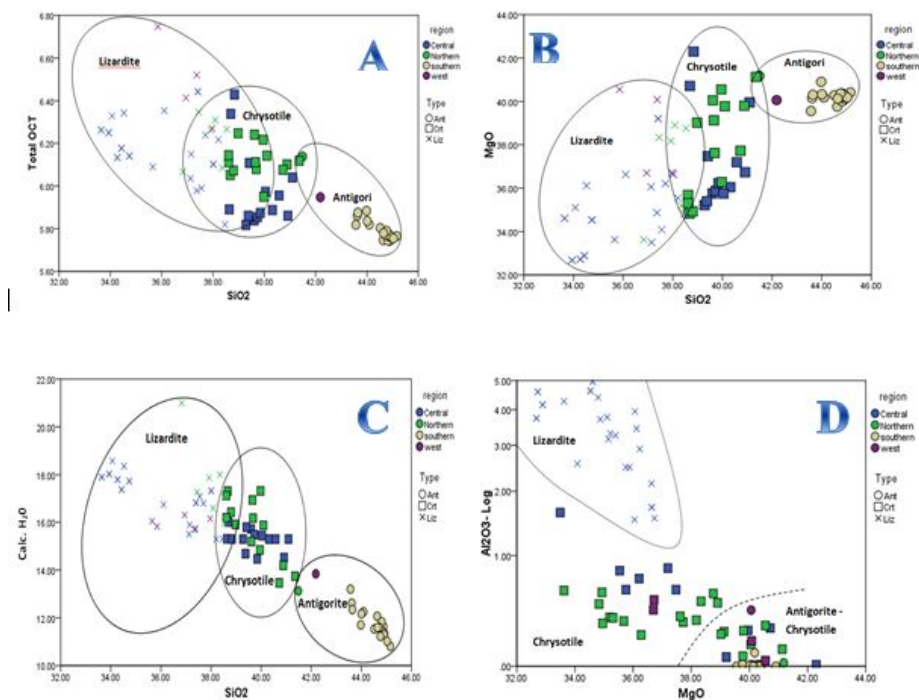
Figure 7. Discriminating diagrams of serpentine polymorphs from the Darepahn area

A) SiO$_2$ versus Σoct diagram, as it revealed antigorites have highest SiO$_2$ and lowest Σoct; lizardites have a reverse position and chrysotiles show moderate composition in this feature.

B) SiO$_2$ versus MgO diagram, lizardites reflected low MgO, antigorites have higher and chrysotiles have a wide range.

C) Total octahedral versus SiO$_2$ diagram, this is one of the best features to separate serpentine polymorphs. Fields plot of antigorite has a comprehensive separation and lizardites have a small common area with chrysotiles.

D) MgO versus Al$_2$O$_3$ diagram, this feature separate lizardites from other polymorphs in best position plot.

MgO versus SiO$_2$, MgO versus Al$_2$O$_3$ and SiO$_2$ versus Calc-H$_2$O. As revealed in Figure 7, Lizardites as primary polymorphs have low SiO$_2$ but high Σoct, Calc-H$_2$O, and Al$_2$O$_3$ that could be results of formation in first metasomatism stages of Olivine enrichment ultramafic complex by an Iron-rich fluid [42]. The minimum overlap field for lizardite separation will be obtained when MgO plotted versus Al$_2$O$_3$ (Fig. 7 d). Chrysotile polymorphs are characterized by higher Σoct than antigorite and much higher SiO$_2$ than lizardite (Fig. 7 a). Both chrysotile and antigorite have higher MgO, SiO$_2$ and Calc-H$_2$O content than lizardite (Table 5 and Fig. 7 b). So MgO, Calc-H$_2$O and SiO$_2$ could be best chemical separator factors to discriminate chrysotile and antigorite from lizardite polymorphs. When SiO$_2$ plotted versus Calc-H$_2$O, we have a comprehensive feature to discriminate antigorite polymorphs (Fig. 7 c). These diagrams are most obtained ideal chemical features to identify serpentine polymorph types of the local study area however, there are some indistinguishable polymorphs that can be considered as hybrid polymorphs in somewhat serpentinized peridotite [34].

Recrystallized Antigorites

The electron microprobe analyses of antigorite presented in Table 3. According to [50], the structural formula of antigorite is highly precise if it is calculated on an anhydrous 14(O) basis and this method is recommended because it eliminates or at least minimizes the Mg^{2+} and OH$^-$ shortages in the alternating wave-structure of antigorite. The cation distribution of antigorite from the studied serpentinites is listed in Table 3 and the obtained structural formula is given as follow:

A $_{5.79}$ Si$_4$ O$_{10}$ (OH)$_8$
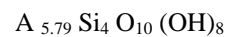
Where A = Mg + Ca + Mn + Fe^{2+}+Ni and trivalent cations occupying the octahedral sites in the antigorite structure.

Antigorites have some recrystallized textures such as deformed fibers and massive cluttered fine grain texture with no detectable relict minerals. There are some significant differences in the structure and composition of antigorite formed by regional metamorphism and recrystallized thermal antigorite [43]. Recrystallized massive antigorites in the Darepahn serpentinites is

Table 3. EMPA of antigorite in serpentinites produced by regional and thermal metamorphism Major oxides in %

Sample	MgO	SiO₂	Al₂O₃	TiO₂	MnO	Cr₂O₃	FeO	CaO	NiO	Na₂O	K₂O	Total
A1	39.558	43.568	0.000	0.000	0.023	0.008	3.471	0.060	0.108	0.000	0.003	86.799
A2	40.907	43.981	0.000	0.000	0.057	0.000	3.186	0.045	0.114	0.010	0.000	88.300
A3	40.184	44.089	0.005	0.015	0.021	0.000	3.199	0.061	0.181	0.000	0.000	87.755
A4	40.327	44.006	0.008	0.011	0.055	0.014	3.153	0.053	0.180	0.007	0.021	87.834
A5	40.061	44.891	0.011	0.000	0.025	0.014	2.867	0.048	0.438	0.009	0.011	88.375
A6	39.763	44.629	0.011	0.000	0.027	0.006	2.923	0.093	0.466	0.007	0.009	87.933
A7	40.285	44.515	0.004	0.008	0.026	0.001	3.003	0.113	0.496	0.009	0.005	88.465
A8	40.367	44.820	0.011	0.000	0.037	0.002	2.894	0.064	0.472	0.018	0.000	88.685
A9	40.412	45.155	0.006	0.000	0.048	0.002	2.961	0.110	0.500	0.000	0.003	89.197
A10	40.279	44.779	0.001	0.000	0.048	0.012	2.766	0.116	0.474	0.012	0.005	88.492
A11	40.152	43.620	0.004	0.000	0.063	0.000	3.363	0.032	0.151	0.001	0.000	87.387
A12	40.302	43.641	0.011	0.000	0.079	0.005	3.449	0.054	0.109	0.006	0.000	87.655
A13	40.009	44.814	0.003	0.005	0.016	0.002	2.768	0.081	0.470	0.000	0.000	88.167
A14	40.223	44.923	0.004	0.000	0.043	0.011	2.889	0.087	0.465	0.006	0.009	88.660
A15	40.158	44.851	0.000	0.000	0.025	0.000	2.962	0.078	0.508	0.000	0.010	88.591
A16	40.167	44.729	0.000	0.000	0.006	0.009	2.942	0.071	0.468	0.002	0.012	88.406
A17	40.299	44.912	0.003	0.013	0.043	0.013	2.909	0.069	0.429	0.014	0.002	88.705
A18	40.181	45.026	0.088	0.000	0.020	0.000	3.104	0.082	0.471	0.002	0.007	88.981
A19	40.368	44.761	0.000	0.000	0.031	0.009	2.994	0.099	0.489	0.003	0.023	88.775
A20	40.131	44.646	0.000	0.000	0.028	0.015	2.983	0.085	0.512	0.000	0.008	88.407

Continue of Table 3, Cations calculated on the basis of 14 oxygen (anhydrous)

Sample	Mg	.Si	Al	Ti	Mn	Cr	Fe	Ca	Ni	An	K	Total OCT
A1	5.529	4.091	0.000	0.000	0.003	0.000	0.272	0.006	0.008	0.000	0.000	5.819
A2	5.619	4.058	0.000	0.000	0.007	0.000	0.245	0.004	0.009	0.002	0.000	5.884
A3	5.549	4.090	0.000	0.001	0.003	0.000	0.248	0.006	0.014	0.000	0.000	5.819
A4	5.567	4.080	0.000	0.000	0.006	0.000	0.244	0.005	0.014	0.001	0.002	5.836
A5	5.483	4.127	0.001	0.000	0.003	0.000	0.220	0.005	0.033	0.002	0.001	5.743
A6	5.473	4.126	0.001	0.000	0.003	0.000	0.226	0.009	0.035	0.001	0.001	5.746
A7	5.521	4.098	0.000	0.000	0.003	0.000	0.231	0.011	0.037	0.002	0.001	5.803
A8	5.511	4.110	0.001	0.000	0.004	0.000	0.222	0.006	0.035	0.003	0.000	5.778
A9	5.486	4.117	0.000	0.000	0.005	0.000	0.225	0.011	0.037	0.000	0.000	5.765
A10	5.508	4.113	0.000	0.000	0.006	0.000	0.212	0.011	0.035	0.002	0.001	5.772
A11	5.577	4.069	0.000	0.000	0.007	0.000	0.262	0.003	0.011	0.000	0.000	5.861
A12	5.584	4.062	0.001	0.000	0.009	0.000	0.268	0.005	0.008	0.001	0.000	5.875
A13	5.486	4.128	0.000	0.000	0.002	0.000	0.213	0.008	0.035	0.000	0.000	5.744
A14	5.491	4.119	0.000	0.000	0.005	0.000	0.221	0.009	0.035	0.001	0.001	5.760
A15	5.489	4.118	0.000	0.000	0.003	0.000	0.227	0.008	0.038	0.000	0.001	5.764
A16	5.501	4.115	0.000	0.000	0.001	0.000	0.226	0.007	0.035	0.000	0.001	5.770
A17	5.499	4.116	0.000	0.000	0.005	0.000	0.223	0.007	0.032	0.002	0.000	5.765
A18	5.472	4.119	0.005	0.000	0.002	0.000	0.237	0.008	0.035	0.000	0.001	5.755
A19	5.511	4.104	0.000	0.000	0.004	0.000	0.229	0.010	0.036	0.000	0.003	5.790
A20	5.500	4.110	0.000	0.000	0.003	0.000	0.229	0.008	0.038	0.000	0.001	5.779
Averege	5.538	4.091	0.002	0.000	0.004	0.000	0.238	0.007	0.027	0.001	0.001	5.814

characterized geochemically by SiO₂ value where it increases, the evidence of recrystallization and higher temperature is increased too. Also, a diagram of NiO versus FeO is a strong distinguishable method to separate thermally recrystallized antigorites from others that produced thru regional metamorphism processes. So in thermal antigorite, NiO is low (less than 0.4 %) and FeO is high (more than 3.1%) whereas in regional antigorite NiO is more than 0.4% and FeO is less than 3.1% (Fig. 8). This occurrence could happen due to more tendency of Ni to staying in former phases through the recrystallization process [44].

The obtained results of cation per formula units in the thermal antigorites, suggest the presence of Tschermak substitutions [45] of Al^{3+} and Cr^{3+} mainly for Mg^{2+} in the octahedral sites and not Si^{4+} in the tetrahedral sites. The sum of Si cations is relatively more value around 4 atoms for thermally than regionally antigorites. So there are not any extra tetrahedral sites here. In contrast, such a type of substitution can be detected in a few regionally originated antigorites with relatively less value of Si atoms. The presence of tetrahedral Tschermak

substitution in regionally originating antigorite and its absence in some samples superimposed by thermal effects is temperature dependent [1]. Based on the collective EMPA data of the studied serpentinites, the metamorphic phases can be predicted which was previously used in other worldwide ophiolitic serpentinites [46]. Dehydration process in same polymorphs can be used as a tracer of the metamorphic phases [1]. This suggests the validity of antigorite as a qualities geo-thermometer. So based on the dehydration process of antigorites, it is confirmed that there were

two metamorphism phases as regional and thermal metamorphic phenomena in the Darepahn ultramafic complex evolution.

Primarily Lizardites

Based on EMPA results represented in Table 4, Lizardite polymorphs in Darepahn serpentinites can consider as primarily metasomatism results [49] by an iron-rich fluid. Lizardite has a relatively high Σoct (more than 5.8) and low Si Cation unites (less than 4) with high Al_2O_3 content. Thus both tetrahedral and

Table 4. EMPA of lizardite in serpentinites produced by regional metamorphism

Sample	MgO	SiO₂	Al₂O₃	TiO₂	MnO	Cr₂O₃	FeO	CaO	NiO	Na₂O	K₂O	Total
L1	34.87	37.36	3.70	0.11	0.17	0.64	7.21	0.13	0.10	0.00	0.01	84.31
L2	32.68	33.94	3.74	0.13	0.23	0.82	9.99	0.32	0.13	0.00	0.01	81.98
L3	32.68	33.94	3.74	0.13	0.23	0.82	9.99	0.32	0.13	0.00	0.01	81.98
L4	36.05	40.31	1.51	0.04	0.16	0.01	6.61	0.09	0.02	0.01	0.00	84.70
L5	36.74	40.92	1.53	0.03	0.06	0.02	6.11	0.04	0.02	0.01	0.00	85.47
L6	35.88	39.73	2.48	0.04	0.16	0.18	5.69	0.34	0.02	0.00	0.00	84.52
L7	35.75	39.60	2.48	0.03	0.17	0.41	5.55	0.26	0.02	0.00	0.01	84.28
L8	36.23	39.84	2.91	0.02	0.12	0.00	6.36	0.05	0.00	0.00	0.01	85.53
L9	35.15	38.63	3.16	0.06	0.14	0.60	6.65	0.25	0.03	0.01	0.00	84.69
L10	35.40	39.38	3.26	0.02	0.08	0.01	7.10	0.05	0.00	0.00	0.01	85.31
L11	35.22	39.28	3.31	0.04	0.13	0.53	6.27	0.20	0.07	0.00	0.01	84.70
L12	34.80	38.47	4.40	0.03	0.09	0.42	6.65	0.10	0.05	0.01	0.00	84.70
L13	34.09	37.55	2.56	0.03	0.24	0.25	7.82	0.31	0.05	0.01	0.01	82.91
L14	36.64	36.10	2.14	0.03	0.16	0.01	7.64	0.16	0.38	0.01	0.00	83.26
L15	34.61	33.64	4.96	0.11	0.19	0.79	7.49	0.17	0.13	0.00	0.00	82.11
L16	34.61	33.64	4.96	0.11	0.19	0.79	7.49	0.17	0.13	0.00	0.00	82.11
L17	36.12	34.53	3.44	0.02	0.16	0.39	6.80	0.13	0.05	0.01	0.00	81.65
L18	35.11	34.07	3.77	0.05	0.17	0.39	7.56	0.24	0.07	0.00	0.00	81.43
L19	36.06	37.12	3.95	0.12	0.12	0.74	6.17	0.09	0.13	0.00	0.00	84.49
L20	32.89	34.43	4.16	0.13	0.19	0.82	9.76	0.17	0.08	0.00	0.00	82.63

Continue of Table 4. Cations calculated on the basis of 14 oxygen (anhydrous)

Sample	Mg	.Si	Al	Ti	Mn	Cr	Fe	Ca	Ni	An	K	TOC
L1	5.3165	3.8259	0.2231	0.0043	0.0222	0.0172	0.6162	0.0147	0.0086	0.0004	0.0009	5.9782
L2	5.2665	3.6736	0.2378	0.0051	0.0320	0.0233	0.9029	0.0370	0.0117	0.0000	0.0014	6.2501
L3	5.2665	3.6736	0.2378	0.0051	0.0320	0.0233	0.9029	0.0370	0.0117	0.0000	0.0014	6.2501
L4	5.3100	3.9885	0.0877	0.0015	0.0197	0.0002	0.5463	0.0095	0.0018	0.0011	0.0004	5.8873
L5	5.3486	4.0016	0.0880	0.0010	0.0079	0.0005	0.4992	0.0039	0.0013	0.0023	0.0000	5.8609
L6	5.3227	3.9588	0.1454	0.0015	0.0206	0.0047	0.4735	0.0361	0.0015	0.0000	0.0000	5.8544
L7	5.3248	3.9616	0.1460	0.0009	0.0213	0.0109	0.4636	0.0279	0.0015	0.0000	0.0008	5.8392
L8	5.3286	3.9357	0.1689	0.0006	0.0150	0.0000	0.5244	0.0055	0.0000	0.0004	0.0008	5.8736
L9	5.2824	3.8993	0.1874	0.0024	0.0183	0.0160	0.5604	0.0267	0.0028	0.0014	0.0005	5.8907
L10	5.2537	3.9251	0.1910	0.0009	0.0102	0.0002	0.5913	0.0051	0.0000	0.0006	0.0014	5.8603
L11	5.2495	3.9328	0.1948	0.0016	0.0170	0.0140	0.5242	0.0209	0.0053	0.0000	0.0018	5.8170
L12	5.2315	3.8841	0.2612	0.0013	0.0120	0.0111	0.5605	0.0110	0.0044	0.0025	0.0000	5.8195
L13	5.2452	3.8812	0.1556	0.0011	0.0319	0.0067	0.6745	0.0343	0.0045	0.0024	0.0008	5.9905
L14	5.6263	3.7240	0.1301	0.0010	0.0207	0.0003	0.6577	0.0177	0.0314	0.0014	0.0000	6.3538
L15	5.5336	3.6121	0.3134	0.0046	0.0264	0.0224	0.6717	0.0196	0.0115	0.0000	0.0001	6.2628
L16	5.5336	3.6121	0.3134	0.0046	0.0264	0.0224	0.6717	0.0196	0.0115	0.0000	0.0001	6.2628
L17	5.6990	3.6589	0.2143	0.0008	0.0218	0.0110	0.6021	0.0145	0.0046	0.0010	0.0000	6.3421
L18	5.5960	3.6473	0.2373	0.0021	0.0236	0.0110	0.6756	0.0276	0.0058	0.0000	0.0000	6.3288
L19	5.4749	3.7852	0.2367	0.0046	0.0154	0.0199	0.5253	0.0094	0.0105	0.0000	0.0001	6.0355
L20	5.2508	3.6922	0.2621	0.0052	0.0263	0.0232	0.8736	0.0196	0.0070	0.0000	0.0000	6.1772
Averege	5.3747	3.7932	0.2115	0.0029	0.0222	0.0134	0.6427	0.0219	0.0083	0.0009	0.0004	6.0698

Table 5. EMPA of chrysotile in serpentinites produced by regional and cataclastic metamorphism

Sample	MgO	SiO₂	Al₂O₃	TiO₂	MnO	Cr₂O₃	FeO	CaO	NiO	Na₂O	K₂O	Total
C1	40.72	38.69	0.27	0.01	0.07	0.00	3.82	0.06	0.34	0.00	0.01	83.99
C2	33.50	37.15	1.62	0.05	0.19	0.42	11.04	0.11	0.04	0.00	0.00	84.10
C3	37.47	39.41	0.62	0.01	0.06	0.00	6.15	0.14	0.35	0.00	0.00	84.20
C4	35.75	40.04	0.62	0.05	0.12	0.04	7.80	0.13	0.01	0.00	0.00	84.56
C5	37.20	40.58	0.85	0.06	0.11	0.03	5.94	0.18	0.02	0.00	0.00	84.70
C6	39.20	37.41	0.06	0.00	0.06	0.00	6.07	0.07	0.31	0.01	0.00	83.19
C7	39.20	37.41	0.06	0.00	0.06	0.00	6.07	0.07	0.31	0.01	0.00	83.19
C8	39.96	41.09	0.25	0.00	0.06	0.00	3.36	0.10	0.06	0.00	0.00	84.70
C9	36.21	37.70	0.73	0.01	0.15	0.00	7.81	0.18	0.41	0.00	0.00	83.20
C10	42.30	38.84	0.01	0.00	0.06	0.01	3.07	0.06	0.36	0.00	0.01	84.70
C11	35.54	38.21	0.82	0.01	0.10	0.00	9.87	0.10	0.31	0.02	0.01	84.70
C12	40.05	39.61	0.15	0.00	0.06	0.00	4.61	0.02	0.31	0.00	0.00	84.80
C13	39.80	40.88	0.25	0.00	0.10	0.00	4.32	0.04	0.40	0.01	0.01	85.80
C14	38.17	37.92	0.33	0.00	0.06	0.01	5.04	0.03	0.57	0.00	0.00	82.13
C15	34.83	38.67	0.48	0.00	0.18	0.00	8.42	0.05	0.05	0.00	0.01	82.69
C16	38.91	38.09	0.49	0.00	0.07	0.02	5.31	0.05	0.47	0.02	0.00	83.41
C17	38.34	37.45	0.50	0.00	0.07	0.00	5.73	0.03	0.61	0.00	0.00	82.73
C18	38.76	38.53	0.58	0.00	0.06	0.01	5.54	0.05	0.50	0.01	0.00	84.04
C19	34.93	38.80	0.59	0.00	0.22	0.00	8.93	0.05	0.05	0.00	0.00	83.57
C20	33.62	36.83	0.61	0.00	0.17	0.00	7.64	0.05	0.06	0.01	0.01	79.00

Continue of Table 5. Cations calculated on the basis of 14 oxygen (anhydrous)

Sample	Mg	.Si	Al	Ti	Mn	Cr	Fe	Ca	Ni	An	K	TOC
C1	5.9822	3.8181	0.0157	0.0004	0.0084	0.0001	0.3144	0.0066	0.0273	0.0000	0.0008	6.3388
C2	5.1564	3.8409	0.0987	0.0019	0.0249	0.0113	0.9529	0.0121	0.0030	0.0000	0.0001	6.1494
C3	5.5472	3.9187	0.0360	0.0002	0.0077	0.0000	0.5103	0.0147	0.0283	0.0000	0.0000	6.1082
C4	5.2954	3.9838	0.0360	0.0018	0.0154	0.0011	0.6477	0.0138	0.0009	0.0000	0.0000	5.9731
C5	5.4353	3.9826	0.0491	0.0021	0.0137	0.0007	0.4866	0.0189	0.0012	0.0000	0.0003	5.9558
C6	5.8910	3.7754	0.0035	0.0000	0.0076	0.0000	0.5117	0.0074	0.0250	0.0027	0.0000	6.4426
C7	5.8910	3.7754	0.0035	0.0000	0.0076	0.0000	0.5117	0.0074	0.0250	0.0027	0.0000	6.4426
C8	5.7464	3.9695	0.0143	0.0000	0.0071	0.0000	0.2712	0.0101	0.0046	0.0000	0.0000	6.0395
C9	5.5008	3.8471	0.0439	0.0003	0.0193	0.0000	0.6651	0.0200	0.0339	0.0000	0.0004	6.2391
C10	6.1375	3.7848	0.0005	0.0000	0.0073	0.0001	0.2496	0.0062	0.0283	0.0000	0.0011	6.4289
C11	5.3369	3.8538	0.0487	0.0003	0.0127	0.0000	0.8315	0.0104	0.0254	0.0029	0.0010	6.2169
C12	5.8306	3.8735	0.0084	0.0000	0.0076	0.0000	0.3761	0.0019	0.0243	0.0000	0.0001	6.2404
C13	5.7072	3.9378	0.0141	0.0000	0.0122	0.0000	0.3472	0.0042	0.0310	0.0021	0.0011	6.1017
C14	5.7764	3.8540	0.0200	0.0000	0.0081	0.0001	0.4277	0.0028	0.0466	0.0004	0.0000	6.2616
C15	5.2997	3.9523	0.0287	0.0000	0.0239	0.0001	0.7182	0.0055	0.0044	0.0003	0.0007	6.0517
C16	5.8131	3.8221	0.0288	0.0000	0.0083	0.0005	0.4446	0.0058	0.0379	0.0037	0.0003	6.3097
C17	5.7981	3.8040	0.0300	0.0000	0.0088	0.0001	0.4858	0.0037	0.0504	0.0000	0.0000	6.3467
C18	5.7517	3.8407	0.0339	0.0000	0.0082	0.0003	0.4612	0.0048	0.0405	0.0015	0.0000	6.2665
C19	5.2777	3.9372	0.0351	0.0000	0.0289	0.0000	0.7565	0.0056	0.0040	0.0003	0.0000	6.0728
C20	5.3512	3.9371	0.0382	0.0000	0.0226	0.0000	0.6824	0.0053	0.0054	0.0023	0.0007	6.0670
Averege	5.6302	3.8799	0.0232	0.0002	0.0136	0.0005	0.5325	0.0070	0.0201	0.0010	0.0003	6.2035

octahedral Tschermak substitutions happened so that Al cations divided between tetrahedral and octahedral sites. An average of 6.04 atom per formula of Σoct (Fig. 7 a and b) suggests a directly proportional relationship of SiO_2 with MgO and reverse proportional relationship of SiO_2 with Σoct. That means that all divalent octahedral cations were decreases except Mg^{2+}. A considerable occupation of total iron (~0.64 cations) is reported in the lizardite structure that could be due to Iron-rich nature of metasomatism fluid [49]. High Iron value is lead to variable Mg^{2+} and SiO_2 with a reverse proportional

relation (Fig. 10). This indicates that Iron is presented in all its tow ionic capacity so that Fe^{2+} in the octahedral sites substituting Mg^{2+} and Fe^{3+} contributed as main trivalent cations along with Al^{3+} and Cr^{3+} in substitution of Si^{4+} in the tetrahedral sites. However, noticed to data distribution of 2D scatter plots (Fig. 10) illustrates a stronger inverse proportional relation between Mg and Fe than Fe and Si. This indicates that more Fe value presented as Fe^{2+} than Fe^{3+}. Fe_2O_3, Al_2O_3, and Cr_2O_3 are inversely related to SiO_2 in the lizardite structure. This reflecting Tschermak substitution of Si^{4+} by R^{3+} (Fe^{3+},

Al^{3+}, and Cr^{3+}) in the tetrahedral sites.

The calculated structural formula of lizardite from the studied area is: $A_{6.07} Si_4 O_{10} (OH)_8$

Overlap of lizardite with other serpentines is limited when SiO_2 is plotted against the calculated H_2O contents (Fig. 7c) and best distinguish will happen when MgO is plotted against Al_2O_3 (Fig. 7d). Hence, the serpentine polymorphs can be discriminated on the binary SiO_2 vs. H_2O and MgO vs. Al_2O_3 diagrams. Despite some overlap in Figure 7c, it can be seen that the structure of chrysotile can accommodate relatively lower silica compared to antigorite. In addition, relative silica depletion is noticed in lizardite and the mineral is very distinguishable from antigorite and chrysotile by its much higher Al and Cr contents (Fig. 9).

Aggregate and Cataclastic Chrysotile

Based on Wicks classifications [30], there are two types of chrysotile that forming in different phases of cataclastic or another type of deformation. In Darepahn serpentinites, we have both these chrysotile phases; Aggregate chrysotile in the groundmass, and Cataclastic chrysotile in the late fractures. Aggregate chrysotile MgO has a normal MgO range (38.34–42.30 wt%) (Fig. 11) whereas the cataclastic chrysotile in the late fractures accepts relatively lower MgO weight percent (33.5–37.73 wt%). This could be due to Mg poor nature of late metasomatism fluids. Si Cation unites value less than 4 illustrated a tetrahedral Tschermak substitution trend in all chrysotile types of the studied area. The relatively high value of Σoct and low Al_2O_3 content in
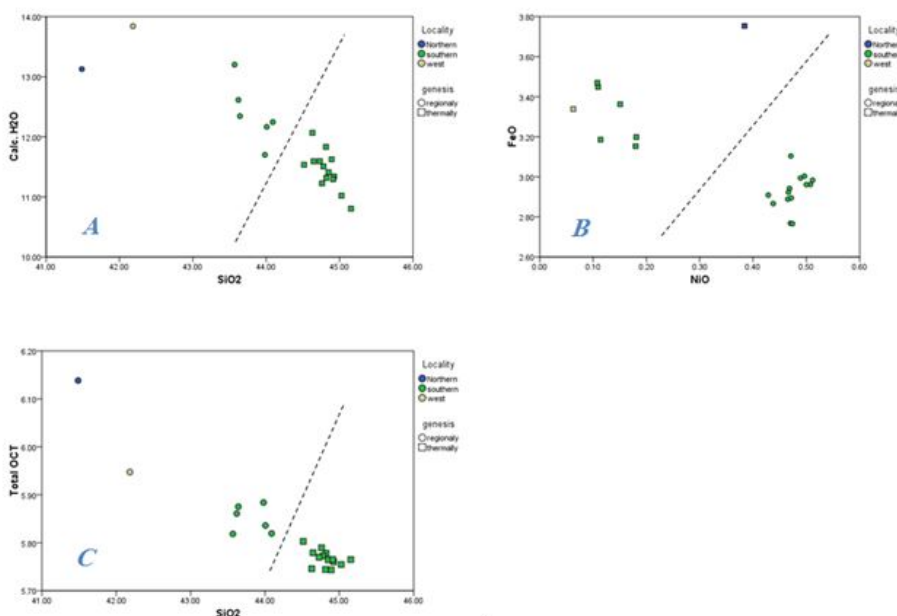
Figure 8. Separator diagrams for Thermal and regional Antigorites in Darepahn serpentinites
A) SiO_2 versus calculated H_2O diagram
B) NiO versus FeO diagram
C) Total octahedral versus SiO_2 diagram.
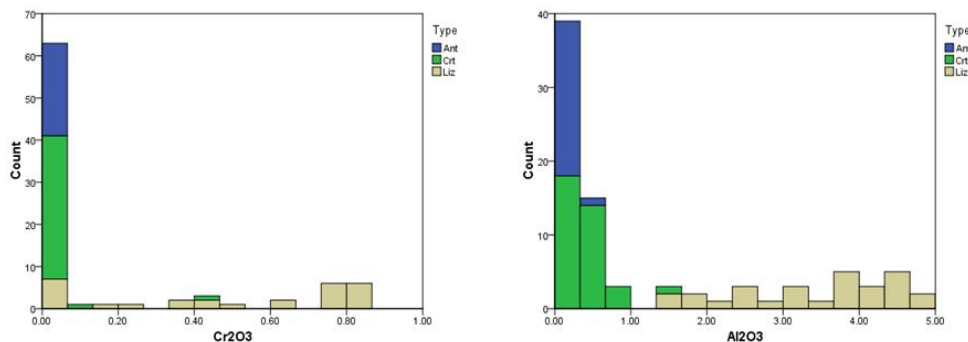
Figure 9. Histograms showing very high contents of Al_2O_3 and Cr_2O_3 in lizardite compared to chrysotile and antigorite in studied serpentinites. Y label is frequency count and X label is weight percent of each oxide.
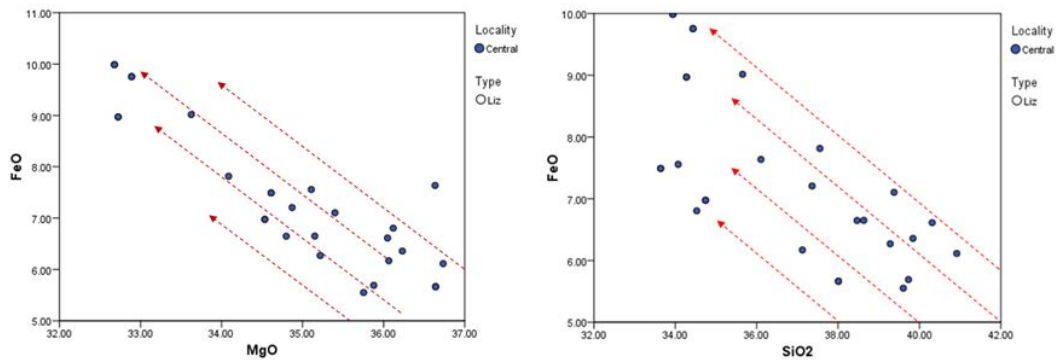
Figure 10. Reverse proportional relationship of FeO by MgO and SiO_2 returned Fe substitution in all its tow ionic capacity of Fe^{2+} in the octahedral sites substituting Mg^{2+} and Fe^{3+} in the tetrahedral position instead of Si^{4+}
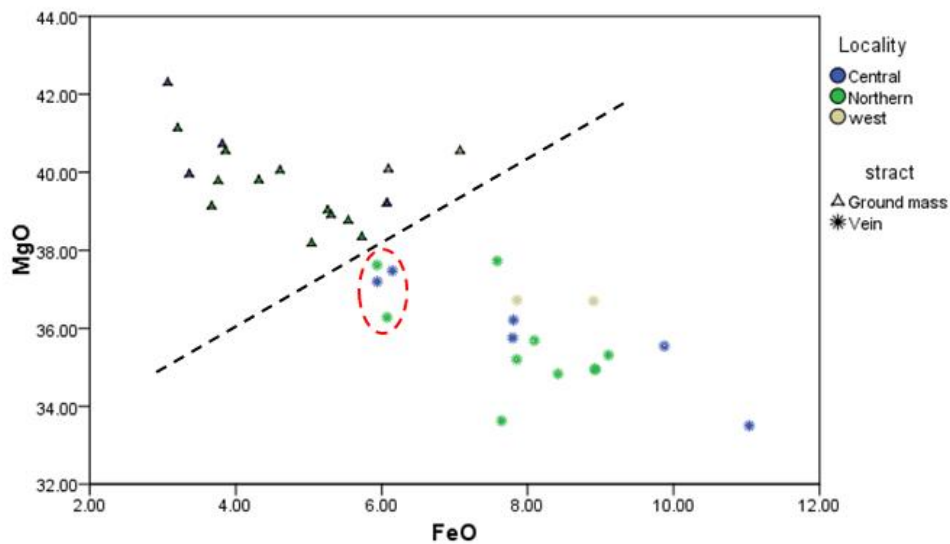

Figure 11. Vein Chrysotiles with low MgO and relatively high FeO against earlier groundmass Chrysotiles; Red oval indicates some late Chrysotiles with lower Fe content due to magnetite formation in veins.

chrysotiles indicates that trivalent cations substituting Si^{4+} in the tetrahedral sites are mostly Fe^{3+}. The calculated structural formulae of Aggregate and Cataclastic chrysotiles from the studied area are:

Aggregate (in the groundmass): A $_{6.18}$ Si_4 O_{10} $(OH)_8$

Cataclastic (in the late fractures): A $_{6.19}$ Si_4 O10 $(OH)_8$

Aggregate chrysotile in the groundmass that co-exists with abundant magnetite is Fe-poor but there is Cataclastic Fe-rich chrysotile in late magnetite-poor veins. Based on [50], progressive and retrogressive temperatures for two consequent events of Aggregate and Cataclastic are 200–300 °C and ≤200 °C, respectively. Magnetite is a sink of Fe^{3+} produced by serpentinization when the primary ferromagnesian minerals break down. Sometimes magnetite was formed

in the veins along with cataclastic chrysotiles (due to some limited local changes on fluid natures), in these cases we encounter to chrysotiles with less FeO content but still enough low MgO content to distinguish from aggregate types (Fig. 11, Red oval).

The occurrence of cataclastic chrysotile represents the last serpentine formed during circulation of oxidizing solutions through the cataclastic fractures [6, 51]. Therefore, cataclastic chrysotile polymorphs have been used as an indicator of fault movements [38]. Diagram of SiO_2 versus MgO discriminate geochemical characteristics of these two types of chrysotile polymorphs in the current study location (Fig. 12). Figure 13 shows SEM imaging of cataclastic chrysotile in sample veins of Darepahn area. The microscopic and SEM investigations suggest the possibility of formation
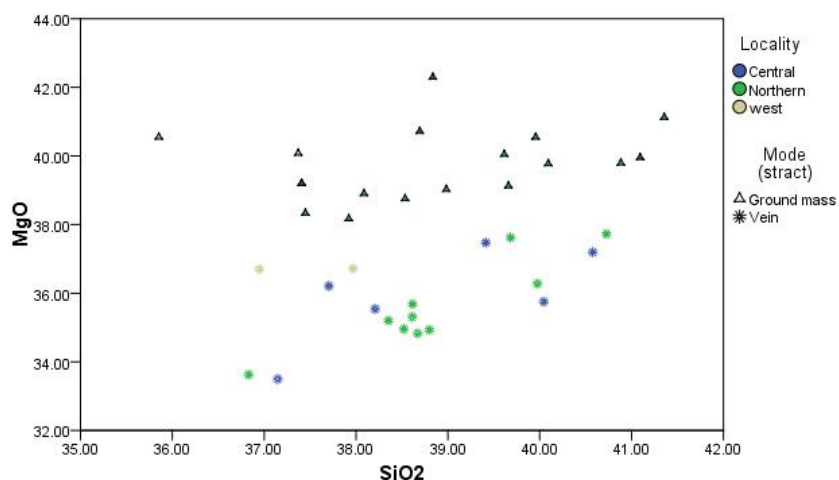
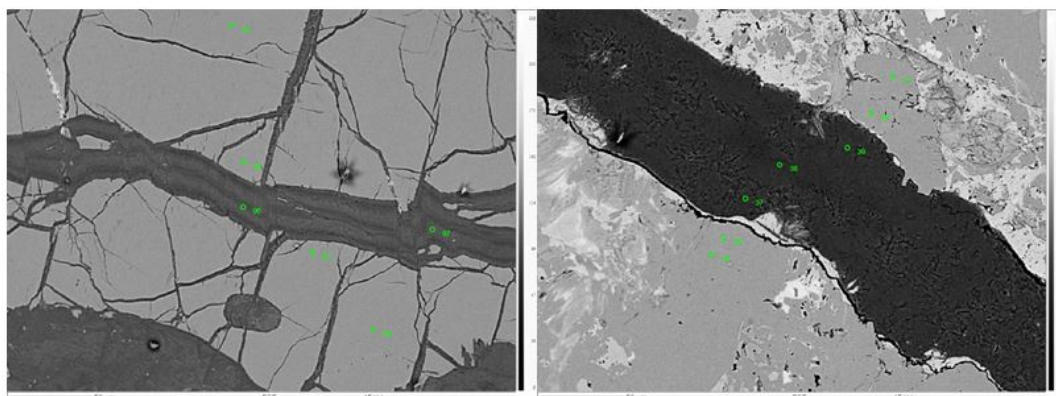**Figure 12.** Discriminate diagram of MgO versus SiO_2 for separating late and former Chrysotiles

Figure 13. SEM images Left: an aggregate chrysotile scene produced in internal tension fractures; Right: a cataclastic Chrysotiles type produced as vine in a fault movement space.

of brucite (Fig. 3g and Fig. 13b) instead of chrysotile in some cross vein serpentinites from the studied area. The present work agrees with [52] that such crack-seal serpentine veins have a range of size from cm to µm scale and they are developed by extensional shearing during hydrothermal alteration (Fig. 13a).

Some major elements including Mg and Fe are highly mobile and removable from primary peridotite to form Fe-rich chrysotile in tension fractures during serpentinization [53]. Accordingly, the additional Iron value can be expected in the structure of chrysotile (5.94–11.04 wt% FeO). Majority of this chrysotile could be represented by polyhedral serpentine according to [54]. This polymorph type form in low temperature (200–300°C), and trivalent cations (R^{3+}) hardly segregate between sheet structures. That means that these minerals were formed in a low grade regional metamorphism in the Darepahn serpentinite. It is

believed that much of iron contents are Fe^{3+} and some excess Mg is concentrated in fractures to form brucite and magnetite (Fig. 3g).

Conclusion

Darepahn serpentinites in the southern part of Iranian inner Zagros ophiolites as a central Alpine-Himalayan Ophiolite complex contain multi-genesis serpentine polymorphs in pseudomorphic (Relict altered Pyroxene and Olivine) and non-pseudomorphic (massive, Fibrous, Dense aggregates and Crack-seal) textures. Raman spectroscopy as an exact experimental technique used to separate serpentine polymorphs by the micro-structural characteristics. Based on local investigations, Raman stock lines that tend to lowest values, generally reflected antigorites, moderate wave numbers were returned to lizardite and highest wave numbers in the defined range were belong to chrysotile.

Whole-rock geochemistry supports Alpine-type hypothesis for target ultramafic rocks and indicates that majority of the studied serpentinites are derived from harzburgite parentages along with some minor lherzolite protolithes that ere belong to a limited district in southern part of the study area.

Data processing of obtained EMPA results of classified serpentine polymorphs discovers different Si and Σoct cation number per formula unites that indicate how distribution cations between tetrahedral and octahedral sheets. Less than 4 Si cations per formulae unite, indicates tetrahedral Tschermak substitution of trivalent cations for Lizardite, whereas, for chrysotile and Antigorite, Tschermak substitutions are octahedrally. These results lead to an important chemical classification so that antigorite has highest SiO_2, and the lowest value of Σoct, Al_2O_3, and Calc-H_2O. In contrast but Lizardite has lowest SiO_2, and the highest value of Σoct, Al_2O_3, and Calc-H_2O. Chrysotile has a moderate chemical composition (between antigorite and lizardite). This important chemical classification for Darepahn serpentine polymorphs presented in so important chemical separator diagrams.

After polymorph classification, we detected tow class in chemical composition features of antigorites with also different textures. Chemical and textural classification of Antigorites (thermally and regionally Antigorites) illustrate significant characteristics as low H_2O (due to dehydration process), high SiO_2 (due to high silica activity in the aureole) and higher Σoct (due to high temperature and Fe^{2+} activity) for thermally-antigorites. We presented discriminate diagrams to distinct this type of antigorites based on EMPA results of antigorites in Darepahn serpentinites.

Lizardite is relative silica depleted phases with bimodal MgO and FeO contents and high Al, Cr and Fe values. Chrysotile occurred in tow whole structural positions depend on the progressive or retrogressive forming situation. Retrograde events occur due to cataclastic deformations in veins. Recent type is along with more Iron contents than ground mass aggregate chrysotiles that return to the process of magnetite formations in groundmass and its absence in late fractures.

Acknowledgements

References

1. Surour A.A., Chemistry of serpentine "polymorphs" in the Pan-African serpentinites from the Eastern Desert of Egypt, with an emphasis on the effect of superimposed thermal metamorphism. *Mineralogy and Petrology*. **111**(1): p. 99-119. (2017).
2. Wu K., Ding X., Ling M.X., Sun W.d., Zhang L.P., Hu Y.B., and Huang R.F., Origins of two types of serpentinites from the Qinling orogenic belt, central China and associated fluid/melt-rock interactions. *Lithos*. **302**: p. 50-64. (2018).
3. Dilek Y., Furnes H., and Shallo M., Geochemistry of the Jurassic Mirdita Ophiolite (Albania) and the MORB to SSZ evolution of a marginal basin oceanic crust. *Lithos*. **100**(1-4): p. 174-209. (2008).
4. Evans B.W., Lizardite versus antigorite serpentinite: Magnetite, hydrogen, and life (?). *Geology*. **38**(10): p. 879-882. (2010).
5. Evans B.W., Hattori K., and Baronnet A., Serpentinite: what, why, where? *Elements*. **9**(2): p. 99-106. (2013).
6. Klein F., Grozeva N.G., Seewald J.S., McCollom T.M., Humphris S.E., Moskowitz B., Berquó T.S., and Kahl W.-A., Experimental constraints on fluid-rock reactions during incipient serpentinization of harzburgite. *American Mineralogist*. **100**(4): p. 991-1002. (2015).
7. Mccollom T.M. and Bach W., Thermodynamic constraints on hydrogen generation during serpentinization of ultramafic rocks. *Geochimica et Cosmochimica Acta*. **73**(3): p. 856-875. (2009).
8. Ohanley D.S., Solution to the volume problem in serpentinization. *Geology*. **20**(8): p. 705-708. (1992).
9. Ulven O., Storheim H., Austrheim H., and Malthe-Sørenssen A., Fracture initiation during volume increasing reactions in rocks and applications for CO2 sequestration. *Earth and Planetary Science Letters*. **389**: p. 132-142. (2014).
10. Müntener O., Serpentine and serpentinization: A link between planet formation and life. *Geology*. **38**(10): p. 959-960. (2010).
11. Müntener O., Hermann J., and Trommsdorff V., Cooling history and exhumation of lower-crustal granulite and upper mantle (Malenco, Eastern Central Alps). *Journal of Petrology*. **41**(2): p. 175-200. (2000).
12. Trommsdorff V. and Evans B.W., Progressive metamorphism of antigorite schist in the Bergell tonalite aureole (Italy). *American Journal of Science*. **272**(5): p. 423-437. (1972).
13. Früh-Green G.L., Connolly J.A., Plas A., Kelley D.S., and Grobety B., Serpentinization of oceanic peridotites: implications for geochemical cycles and biological activity. *The subseafloor biosphere at mid-ocean ridges*: p. 119-136. (2004).
14. Jones L.C., Rosenbauer R., Goldsmith J.I., and Oze C., Carbonate control of H2 and CH4 production in serpentinization systems at elevated P-Ts. *Geophysical Research Letters*. **37**(14). (2010).
15. Godard M., Lagabrielle Y., Alard O., and Harvey J.,

Geochemistry of the highly depleted peridotites drilled at ODP Sites 1272 and 1274 (Fifteen-Twenty Fracture Zone, Mid-Atlantic Ridge): Implications for mantle dynamics beneath a slow spreading ridge. *Earth and Planetary Science Letters*. **267**(3): p. 410–425. (2008).

16. Shafii Moghadam H., Stern R.J., and Rahgoshay M., The Dehshir ophiolite (central Iran): Geochemical constraints on the origin and evolution of the Inner Zagros ophiolite belt. *Bulletin*. **122**(9-10): p. 1516-1547. (2010).

17. Delaloye M. and Desmons J., Ophiolites and mélange terranes in Iran: a geochronological study and its paleotectonic implications. *Tectonophysics*. **68**(1-2): p. 83–111. (1980).

18. Ghazi M. and Hassanipak A., Petrology and geochemistry of the Shahr-Babak ophiolite, Central Iran. *Geology society of America*. **61**: p. 485–498. (2000).

19. Shahabpour J., Island-arc affinity of the Central Iranian volcanic belt. *Journal of Asian Earth Sciences*. **30**(5-6): p. 652-665. (2007).

20. Shafaii-Moghadam H., The Naien-Baft ophiolites: An evidence of back-arc basin spreading in the active margin of the Iranian continent. *Geophysical Research Abstracts*. **9**: p. 791. (2007).

21. Lanphere M.A. and Pamić J., 40Ar39Ar ages and tectonic setting of ophiolite from the Neyriz area, southeast Zagros Range, Iran. *Tectonophysics*. **96**(3-4): p. 245-256. (1983).

22. Babaie H., Ghazi A., Babaei A., La Tour T., and Hassanipak A., Geochemistry of arc volcanic rocks of the Zagros Crush Zone, Neyriz, Iran. *Journal of Asian Earth Sciences*. **19**(1-2): p. 61–76. (2001).

23. Hacker B., Mosenfelder J., and Gnos E., Rapid emplacement of the Oman ophiolite: Thermal and geochronologic constraints. *Tectonics*. **15**(6): p. 1230-1247. (1996).

24. Shafaii Moghadam H., The Nain-Baft Ophiolites (Central Iran): Age. *Structure and Origin [Ph. D. thesis]: Tehran, Iran, Shahid Beheshti University*. (2009).

25. Sabzehei M. and Watters M., Preliminary report on the geology and petrography of the metamorphic and igneous rocks of central part of Neiriz. *Geological Survey of Iran*: p. 106–119. (1970).

26. Lagabrielle Y. and Lemoine M., Alpine, Corsican and Apennine ophiolites: the slow-spreading ridge model. *Comptes Rendus de l'Académie des Sciences-Series IIA-Earth and Planetary Science*. **325**(12): p. 909-920. (1997).

27. Mukasa S.B. and Ludden J.N., Uranium-lead isotopic ages of plagiogranites from the Troodos ophiolite, Cyprus, and their tectonic significance. *Geology*. **15**(9): p. 825-828. (1987).

28. Ahmadipour H., Sabzehei M., Emami M., Whitwchurch H., and Pastad E., Soghan complex as an evidence for paleospreading center and mantle diapirism in Sanandaj-Sirjan zone (south-east Iran). (2003).

29. Petriglieri J., Salvioli-Mariani E., Mantovani L., Tribaudino M., Lottici P., Laporte-Magoni C., and Bersani D., Micro Raman mapping of the polymorphs of serpentine. *Journal of Raman Spectroscopy*. **46**(10): p. 953-958. (2015).

30. Wicks F. and O'Hanley D.S., Serpentine minerals; structures and petrology. *Reviews in Mineralogy and Geochemistry*. **19**(1): p. 91-167. (1988).

31. Page N.J., Serpentinization in a sheared serpentinite lens, Tiburon Peninsula, California. *US Geological Survey Professional Paper*. **600**: p. 21-28. (1968).

32. Viti C. and Mellini M., Mesh textures and bastites in the Elba retrograde serpentinites. *European Journal of Mineralogy*. **10**(6): p. 1341-1359. (1998).

33. Piccardo G.B. and Guarnieri L., Alpine peridotites from the Ligurian Tethys: an updated critical review. *International Geology Review*. **52**(10-12): p. 1138-1159. (2010).

34. Schwarzenbach E.M., Gazel E., and Caddick M.J., Hydrothermal processes in partially serpentinized peridotites from Costa Rica: evidence from native copper and complex sulfide assemblages. *Contributions to Mineralogy and Petrology*. **168**(5): p. 1079. (2014).

35. Rinaudo C., Belluso E., and Gastaldi D., Assessment of the use of Raman spectroscopy for the determination of amphibole asbestos. *Mineralogical Magazine*. **68**(3): p. 455-465. (2004).

36. Weber I., Böttger U., Pavlov S., Jessberger E., and Hübers H. W., Mineralogical and Raman spectroscopy studies of natural olivines exposed to different planetary environments. *Planetary and Space Science*. **104**: p. 163-172. (2014).

37. Rinaudo C., Gastaldi D., and Belluso E., Characterization of chrysotile, antigorite and lizardite by FT-Raman spectroscopy. *The Canadian Mineralogist*. **41**(4): p. 883-890. (2003).

38. Whittaker E. and Wicks F., Chemical differences among serpentine polymorphs-A discussion. *Academy of management review*. **55**(5-6). (1970).

39. Whittaker E. and Zussman J., The characterization of serpentine minerals by X-ray diffraction. *Mineralogical Magazine*. **31**(233): p. 107-126. (1956).

40. Schwarzenbach E.M., Caddick M.J., Beard J.S., and Bodnar R.J., Serpentinization, element transfer, and the progressive development of zoning in veins: evidence from a partially serpentinized harzburgite. *Contributions to Mineralogy and Petrology*. **171**(1): p. 5. (2016).

41. Iyer K., Mechanisms of serpentinization and some geochemical effects. *University of Oslo* **111**. (2007).

42. Wicks F.J., Deformation histories as recorded by serpentinites; II, Deformation during and after serpentinization. *The Canadian Mineralogist*. **22**(1): p. 197-203. (1984).

43. Bromiley G.D. and Pawley A.R., The stability of antigorite in the systems MgO-SiO2-H2O (MSH) and MgO-Al2O3-SiO2-H2O (MASH): The effects of Al3+ substitution on high-pressure stability. *American Mineralogist*. **88**(1): p. 99-108. (2003).

44. Wunder B., Wirth R., and Gottschalk M., Antigorite pressure and temperature dependence of polysomatism and water content. *European Journal of Mineralogy*. **13**(3): p. 485-496. (2001).

45. Padrón-Navarta J.A., Sánchez-Vizcaíno V.L., Hermann J., Connolly J.A., Garrido C.J., Gómez-Pugnaire M.T., and Marchesi C., Tschermak's substitution in antigorite and consequences for phase relations and water liberation in high-grade serpentinites. *Lithos*. **178**: p. 186-196. (2013).

46. Mellini M., Cressey G., Wicks F., and Cressey B., The crystal structure of Mg end-member lizardite-1 T forming

polyhedral spheres from the lizard, Cornwall. *Mineralogical Magazine*. **74**(2): p. 277–284. (2010).

47. Mellini M., Chrysotile and polygonal serpentine from the Balangero serpentinite. *Mineral Mag*. **50**: p. 301-306. (1986).

48. Mellini M., Trommsdorff V., and Compagnoni R., Antigorite polysomatism: behaviour during progressive metamorphism. *Contributions to Mineralogy and Petrology*. **97**(2): p. 147-155. (1987).

49. Andréani M., Mével C., Boullier A.M., and Escartin J., Dynamic control on serpentine crystallization in veins: Constraints on hydration processes in oceanic peridotites. *Geochemistry, Geophysics, Geosystems*. **8**(2). (2007).

50. Klein F., Bach W., Humphris S.E., Kahl W.-A., Jöns N., Moskowitz B., and Berquó T.S., Magnetite in seafloor serpentinite—Some like it hot. *Geology*. **42**(2): p. 135-138. (2014).

51. Cressey G., Cressey B., and Wicks F., The significance of the aluminium content of a lizardite at the nanoscale: the role of clinochlore as an aluminium sink. *Mineralogical Magazine*. **72**(3): p. 817-825. (2008).

52. Andreani M., Baronnet A., Boullier A.-M., and Gratier J.-P., A microstructural study of a "crack-seal" type serpentine vein using SEM and TEM techniques. *European Journal of Mineralogy*. **16**(4): p. 585-595. (2004).

53. Evans B.W., Stability of chrysotile and antigorite in the serpentine multisystem. *Schweiz Mineral Petrogr Mitt*. **56**: p. 79-93. (1976).

54. Andreani M., Grauby O., Baronnet A., and Muñoz M., Occurrence, composition and growth of polyhedral serpentine. *European Journal of Mineralogy*. **20**(2): p. 159-171. (2008).

55. Whitney D.L. and Evans B.W., Abbreviations for names of rock-forming minerals. *American mineralogist*. **95**(1): p. 185-187. (2010).